

Comment on “Resolving spatial and energetic distributions of trap states in metal halide perovskite solar cells”

Sandheep Ravishankar,¹ Thomas Unold² and Thomas Kirchartz^{1,3*}

¹IEK-5 Photovoltaik, Forschungszentrum Jülich, 52425 Jülich, Germany

²Department of Structure and Dynamics of Energy Materials, Helmholtz-Zentrum-Berlin, Hahn-Meitner-Platz 1, 14109 Berlin, Germany

³Faculty of Engineering and CENIDE, University of Duisburg-Essen, Carl-Benz-Str. 199, 47057 Duisburg, Germany

*author for correspondence, email: t.kirchartz@fz-juelich.de

Abstract

Ni et al. report minimum bulk trap densities of 10^{11} cm^{-3} and 1-4 orders change in interfacial trap densities derived from drive-level capacitance profiling of lead halide perovskites. From basic electrostatic arguments, we show that such bulk trap densities cannot be resolved for a p-i-n perovskite solar cell for the reported layer thicknesses, while the apparent interfacial charge densities are a consequence of the geometrical capacitance and of charge injection into the perovskite layer.

Despite the excellent optoelectronic properties of lead-halide perovskites, efforts to better understand the details of the remaining losses due to non-radiative recombination via defects are crucial to further improve the performance of photovoltaic or light emitting devices.(1-3) While many publications study the impact of defects on observable parameters such as photoluminescence quantum yields or lifetimes extracted from transient experiments, only few methods(4, 5) allow the determination of the energetic depth of a trap and its spatial position. One method that has been shown to allow achieving both is the so-called drive-level capacitance profiling (DLCP) method that has previously been applied to amorphous Si(6), CdTe(7) and Cu(In,Ga)Se₂ solar cells.(8) Ni et al.(9) recently introduced the DLCP method to the halide perovskite community to resolve bulk trap densities as low as $\sim 10^{11} \text{ cm}^{-3}$ (Fig. 1F, Fig. 2B, Fig. 3A in ref. (9)). In addition, the authors resolve interfacial trap densities that increase by 1-4 orders of magnitude from bulk values (Fig. 1F, Fig. 2D, Fig. 3A, Fig. 4B in ref. (9)). However, a charge density can only be detected in capacitance measurements if it sufficiently affects the electrostatic potential, which requires either sufficiently high charge densities, low permittivities or sufficient thicknesses.(10) If charge densities are too low, spatial resolution will be lost. Using basic electrostatic arguments, we will show that capacitance-based methods unfortunately cannot resolve the charge densities observed in ref. (9), except for the measurement shown in Fig. 1E. In addition, we will show that perovskite solar cells without any defects or dopant atoms will show a behaviour that closely resembles the one in ref. (9), indicating a threshold value below which the response cannot be considered to originate from a density of defects or dopants. This threshold value is universal and can be analytically calculated.

The inherent assumption required to obtain spatial information in capacitance profiling methods such as capacitance-voltage (CV) and DLCP measurements is the existence of a space-charge region of width w generated by a charge density N_d (dopant or trap densities) within the device of thickness d , that can be modified by the applied voltage V . Upon applying a perturbation, a response is obtained from the edge of the depletion region or from a density of emission-limited traps located at the junction transition region.(8, 11) Therefore, though DLCP

is not a small perturbation technique like a CV measurement, the electrostatic origin of the response is identical. Indeed, the two techniques yield very similar results, especially at low frequencies where the deep traps respond.⁽⁸⁾ We use this property to illustrate the limitations of the DLCP technique to resolve charge densities, from numerical simulations of CV measurements of intrinsic p-i-n perovskite solar cells using SCAPS.⁽¹²⁾ A common representation is the doping density profile, which is a plot of $N_d(w) = -2(dC^{-2}/dV)^{-1}/q\varepsilon_r\varepsilon_0$ versus profiling distance $w = \varepsilon_r\varepsilon_0/C(V)$, where C is the capacitance per unit area (Fcm^{-2}), ε_r and ε_0 are the relative permittivity of the perovskite and permittivity of free space respectively and q is the elementary charge. A simulated doping profile is shown in Fig. 1A for a reference p-i-n type perovskite solar cell (parameters and band diagram in Table S1 and Fig. S1 respectively) devoid of any dopant or trap densities for the same thicknesses used in Fig. 3A of ref. (9). The apparent doping profile is ‘U’-shaped and is nearly identical to the spatial trap density profile reported in Fig. 3A of ref. (9). A similar effect is observed in Fig. 1B for an intrinsic and trap-free thin film solar cell, though the apparent doping densities are a few orders of magnitude higher. These doping profiles can be understood from the relation between a Mott-Schottky plot (C^{-2} versus V) and a doping profile, shown in Fig. S2. The rise in the apparent dopant densities at the interfaces are simply the plateaus at low and high forward bias of the Mott-Schottky plots (see Fig. S3), while the apparent doping density in the bulk corresponds to the linear apparent Mott-Schottky regime. Such a shape of the Mott-Schottky profile is actually a fundamental response due to the combination of a geometrical capacitance of the electrodes combined with charge injection into the absorber layer. Charge injection at forward bias in a diode typically leads to an exponentially voltage dependent capacitance that is sometimes called diffusion capacitance or chemical capacitance.⁽¹³⁾ If we connect this voltage dependent capacitance in parallel to a geometric capacitance (i.e. $C = C_g + C_0 \exp(qV/mk_B T)$), the shape of the doping profiles can be analytically calculated (see section A1 and A2 in the supplementary materials).

The above observations are significant due to the fact that if the doping/trap densities are not high enough to affect the electric field of the intrinsic perovskite layer or if the absorber layer thickness, d , is too small, the condition $w \leq d$ is not satisfied over most if not all of the voltage range used. For example, for the lowest reported bulk trap densities of $\sim 10^{11} \text{ cm}^{-3}$ in $\sim 39 \mu\text{m}$ thick perovskite layers in ref. (9), the theoretical space-charge layer width at the onset of the linear Mott-Schottky region would be $w = 88.5 \mu\text{m}$, i.e. much larger than the crystal thickness. In such situations, the geometric and injection capacitances dominate the response and yield a minimum charge density (derived in section A2 in supplementary materials) given by

$$N_{d,\min} = 27mk_B T \varepsilon_r \varepsilon_0 / 4q^2 d^2. \quad (1)$$

This forms the plateau region of the doping profile and only measured charge densities greater than this limit can be considered as a response from doping or from charged defects. This limit is shown in Fig.1C for different relative permittivities, yielding a value of $\sim 3.8 \times 10^{11} \text{ cm}^{-3}$ for a $39 \mu\text{m}$ perovskite layer with $\varepsilon_r = 30$, slightly higher than the measured minimum charge densities in ref. (9). Since the minimum charge density is inversely proportional to the square of the thickness of the device, intrinsic thin films will always show larger apparent doping/trap densities than bulk single crystal films. This is indeed observed experimentally as shown in Fig. S10B in ref. (9). Furthermore, as mentioned earlier, the apparent rise in interfacial charge densities is a direct consequence of charge injection, which can be analytically described by $N_d(w) = mk_B T \varepsilon_r \varepsilon_0 / q^2 w^2$ (see section A1 in the supplementary materials) and is indeed universally observed for DLCP or CV measurements of many different photovoltaic technologies as seen in Fig. 2. Therefore, we recommend that only charge densities in the plateau region of the doping profile (such as seen in Fig. 1E of ref. (9)) be considered as representing dopant/trapped charge densities, given that they are larger than the minimum charge densities derived from Eq.1.

Supplementary Materials

Table S1

Fig. S1-S7

Section A1-A2

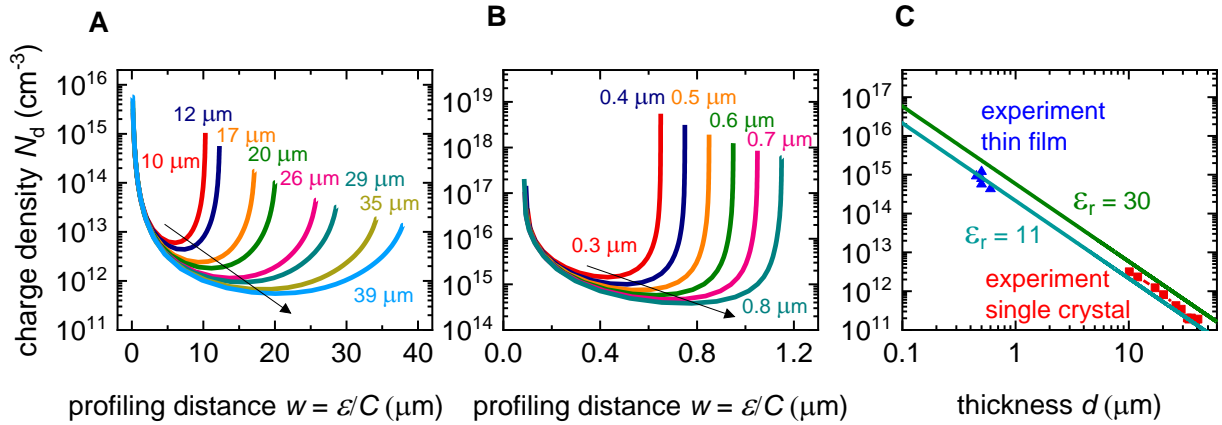


Fig. 1. Doping profiles and minimum charge densities required for resolution in bulk single crystal and polycrystalline thin film trap-free, dopant-free perovskite solar cells. Simulated spatial doping profiles at 10^3 Hz of a p-i-n type PTAA (10 nm)/perovskite/PCBM (25 nm) solar cell for (A) same thicknesses as used in Fig. 3A in ref. (9) of the bulk perovskite layer. Arrow indicates reduction of apparent bulk charge (dopant or trap) densities with increasing thickness. The profile is identical to Fig. 3A in ref. (9) even with the absence of any dopant or trap densities in the model. (B) Different thicknesses between 300-800 nm representative of perovskite thin films. Arrow indicates apparent reduction of bulk charge densities with thickness. (C) Minimum charge densities (dopant or trap) that will be observed in a capacitance-voltage measurement ($m = 2$ is assumed) for different thicknesses and permittivities typical of perovskite (olive) and silicon or organic (cyan) solar cells, in comparison with measured minimum charge densities reported for bulk single crystal and polycrystalline thin films in ref. (9).

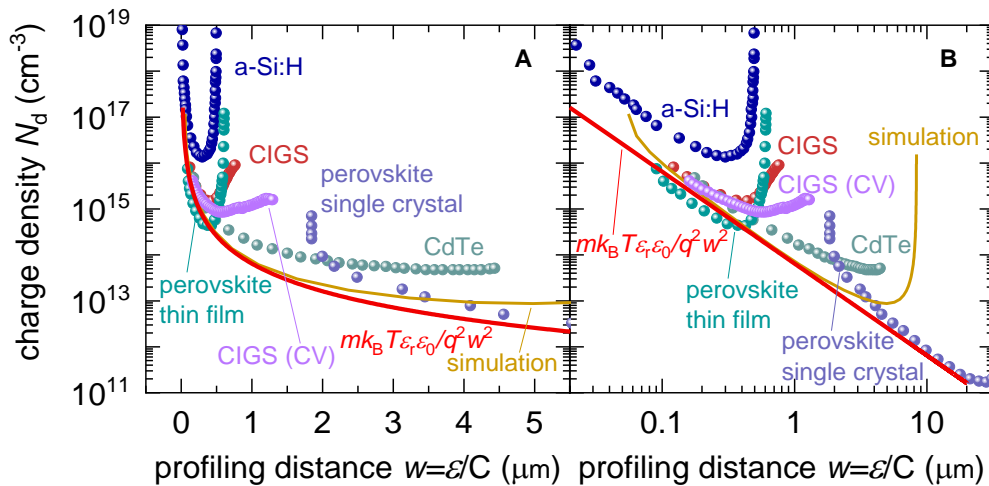


Fig. 2. Universal rise in apparent interfacial charge densities due to charge injection. Some reported spatial trap profiles shown with (A) linear and (B) logarithmic horizontal axis obtained from DLCP and CV measurements for different solar cell technologies such as amorphous hydrogenated silicon (a-Si:H), (14) copper indium gallium selenide ($\text{CuIn}_x\text{Ga}_{1-x}\text{Se}_2$ - CIGS), (15, 16) methylammonium lead iodide perovskite, (9) cadmium telluride (CdTe), (7) and an 8 μm thick p-i-n perovskite solar cell simulated using SCAPS. Also plotted is the analytical formula (with $m = 1.5$ and $\epsilon_r = 30$) derived by considering a geometric capacitance in parallel with an exponential injection capacitance (see section A1 in the supplementary materials). The

capacitance related to injection of charge at forward bias causes an apparent rise in the interfacial charge densities at the lowest profiling distances (left side of ‘U’-shaped profile in A) that can erroneously be interpreted as trap densities. The geometric capacitance gives the corresponding rise in interfacial charge densities at maximum profiling distances (right side of ‘U’-shaped profile in A). B clearly shows the universality in the doping profiles of different types of solar cells at forward bias due to the injection capacitance.

References

1. D. Luo, R. Su, W. Zhang, Q. Gong, R. Zhu, Minimizing Non-Radiative Recombination Losses in Perovskite Solar Cells. *Nat. Rev. Mater.* **5**, 44-60 (2020).
2. I. L. Braly *et al.*, Hybrid Perovskite Films Approaching the Radiative Limit with Over 90% Photoluminescence Quantum Efficiency. *Nat. Photonics* **12**, 355-361 (2018).
3. S. G. Motti *et al.*, Defect Activity in Lead Halide Perovskites. *Adv. Mater.* **31**, 1901183 (2019).
4. T. A. Doherty *et al.*, Performance-Limiting Nanoscale Trap Clusters at Grain Junctions in Halide Perovskites. *Nature* **580**, 360-366 (2020).
5. S. Draguta *et al.*, Spatially Non-Uniform Trap State Densities in Solution-Processed Hybrid Perovskite Thin Films. *J. Phys. Chem. Lett.* **7**, 715-721 (2016).
6. C. Michelson, A. Gelatos, J. Cohen, Drive-Level Capacitance Profiling: Its Application to Determining Gap State Densities in Hydrogenated Amorphous Silicon Films. *Appl. Phys. Lett.* **47**, 412-414 (1985).
7. D. Menossi, E. Artegiani, A. Salavei, S. Di Mare, A. Romeo, Study of MgCl₂ Activation Treatment on the Defects of CdTe Solar Cells by Capacitance-Voltage, Drive Level Capacitance Profiling and Admittance Spectroscopy Techniques. *Thin Solid Films* **633**, 97-100 (2017).
8. J. T. Heath, J. D. Cohen, W. N. Shafarman, Bulk and Metastable Defects in CuIn_{1-x}Ga_xSe₂ Thin Films using Drive-Level Capacitance Profiling. *J. Appl. Phys.* **95**, 1000-1010 (2004).
9. Z. Ni *et al.*, Resolving Spatial and Energetic Distributions of Trap States in Metal Halide Perovskite Solar Cells. *Science* **367**, 1352-1358 (2020).
10. T. Kirchartz *et al.*, Sensitivity of the Mott-Schottky Analysis in Organic Solar Cells. *J. Phys. Chem. C* **116**, 7672-7680 (2012).
11. L. Kimerling, Influence of Deep Traps on the Measurement of Free-Carrier Distributions in Semiconductors by Junction Capacitance Techniques. *J. Appl. Phys.* **45**, 1839-1845 (1974).
12. M. Burgelman, P. Nollet, S. Degraeve, Modelling Polycrystalline Semiconductor Solar Cells. *Thin solid films* **361**, 527-532 (2000).
13. S. M. Sze, K. K. Ng, *Physics of Semiconductor Devices* (John Wiley & sons, 2006), pp.100-102.
14. R. S. Crandall, J. Yang, S. Guha, Defect Density Profiling in Light-Soaked and Annealed Hydrogenated Amorphous Silicon Solar Cells. *Mater. Res. Soc. Symp. Proc.* **664**, A19.2 (2001).

15. L. M. Mansfield *et al.*, Comparison of CIGS Solar Cells Made with Different Structures and Fabrication Techniques. *IEEE J. Photovolt.* **7**, 286-293 (2016).
16. T. Eisenbarth, T. Unold, R. Caballero, C. A. Kaufmann, H.-W. Schock, Interpretation of Admittance, Capacitance-Voltage, and Current-Voltage Signatures in Cu(In, Ga)Se₂ Thin Film Solar Cells. *J. Appl. Phys.* **107**, 034509 (2010).

Acknowledgements

SR and TK acknowledge funding from the Helmholtz Association via the project PEROSEED.

Supplementary Materials for
Comment on “Resolving spatial and energetic distributions of trap states in metal halide perovskite solar cells”

Sandheep Ravishankar,¹ Thomas Unold² and Thomas Kirchartz^{1,3*}

¹IEK-5 Photovoltaik, Forschungszentrum Jülich, 52425 Jülich, Germany

²Department of Structure and Dynamics of Energy Materials, Helmholtz-Zentrum-Berlin, Hahn-Meitner-Platz 1, 14109 Berlin, Germany

³Faculty of Engineering and CENIDE, University of Duisburg-Essen, Carl-Benz-Str. 199, 47057 Duisburg, Germany

*author for correspondence, email: t.kirchartz@fz-juelich.de

Table S1 Parameters used for the simulations in the main text and supplementary materials.

parameter	PTAA	perovskite	PCBM
thickness (nm)	10 nm	variable	25 nm
relative permittivity	3	30	3
bandgap (eV)	3.2	1.58	2
electron affinity (eV)	2.22	3.93	4.05
effective DOS CB (cm ⁻³)	2 × 10 ¹⁸	2 × 10 ¹⁸	2 × 10 ¹⁸
effective DOS VB (cm ⁻³)	2 × 10 ¹⁸	2 × 10 ¹⁸	2 × 10 ¹⁸
radiative recombination coefficient (cm ³ /s)	0	6 × 10 ⁻¹¹	0
electron mobility (cm ² /Vs)	10 ⁻³	20	10 ⁻³
hole mobility (cm ² /Vs)	10 ⁻³	20	10 ⁻³
doping density (cm ⁻³)	0	0	0

Discussion of the parameters

Metal contacts: The metal contact workfunctions chosen were 5.2 eV (ITO) for the PTAA layer side based on ref. (1) and 4.2 eV (Ag) for the PCBM layer side to obtain a built-in voltage of 1 V. The surface recombination velocities for electrons and holes at both metal contacts was set to 10⁷ cm/s.

Thickness: The thicknesses were chosen based on ref. (2).

Relative permittivity: The relative permittivity value for the PTAA and PCBM layers was set to 3 since typical values for fullerenes lie between 2 and 4.(3) The value for the perovskite layer relative permittivity was chosen based on ref. (4).

Bandgap: The PTAA layer bandgap was chosen from ref. (5). The perovskite layer considered was a CH₃NH₃PbI₃ perovskite with a bandgap of ~1.58 eV.(6) The PCBM layer bandgap was chosen based on ref. (7).

Electron affinities: The electron affinity of the PTAA layer was chosen from ref. (8). The PCBM layer electron affinity was set to 4.05 eV based on the different values reported (3.7 and

4.2 eV(9, 10)) and considering the Ag work function of 4.2 eV. The perovskite layer electron affinity was increased from 3.83 eV (obtained from ref. (5)) to 3.93 eV to reduce the barrier for electrons at the perovskite/PCBM interface.

Effective density of states (DOS): The effective DOS for the conduction and valence band of the perovskite layer was chosen from ref. (11). The DOS of the PCBM and PTAA layers were chosen to be the same as that of the perovskite layer.

Radiative recombination coefficient: The order of the perovskite layer radiative recombination coefficient was chosen from ref. (11). No recombination in the PCBM and PTAA layers was assumed.

Mobility: We fixed the electron and hole mobilities to be equal in all cases for simplicity. Based on the generally large mobilities reported for perovskite layers, we fixed a value of 20 cm^2/Vs .(12) For the PCBM layer, the value was chosen based on ref. (13). The PTAA layer mobility was chosen based on ref. (14).

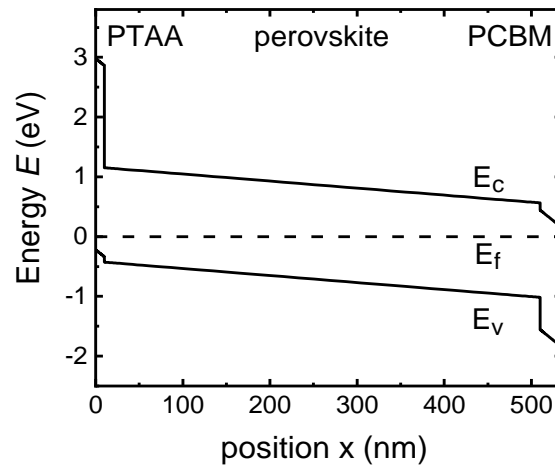


Fig. S1. Reference band diagram. Band diagram of a reference PTAA (10 nm)/ $\text{CH}_3\text{NH}_3\text{PbI}_3$ perovskite (500 nm)/ PCBM (25 nm) stack.

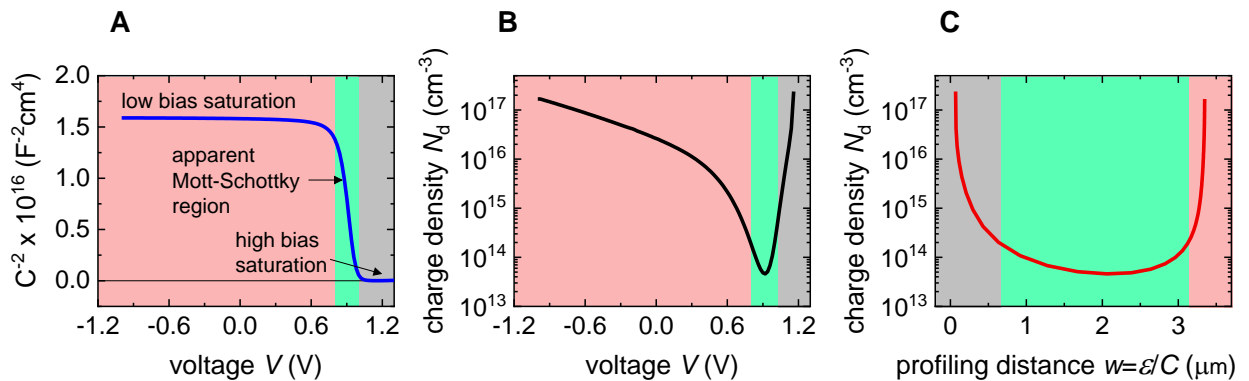


Fig. S2. Connection between the Mott-Schottky plot and doping profile plot. (A) Simulated Mott-Schottky plot of a p-i-n type PTAA (10 nm)/ perovskite (3 μm)/ PCBM (25 nm) solar cell with its corresponding apparent doping profile versus voltage shown in (B) and versus profiling

distance shown in (C). The Mott-Schottky plot is linear at intermediate voltages while saturating to an almost constant value at forward and reverse bias as shown. The doping profile is proportional to the inverse slope of the Mott-Schottky plot, given by $N_d(V) = -2(dC^{-2}/dV)^{-1}/q\epsilon_r\epsilon_0$. This is shown as a function of voltage in B. However, a common representation to obtain spatial information is plotting the x-axis as the profiling distance w given by $w = \epsilon_r\epsilon_0/C(V)$. This is shown in C, where peaks are formed in the saturation regimes of A corresponding to apparent maximum and minimum profiling distances (i.e.: interfaces of the perovskite) and a plateau-like evolution in the apparent Mott-Schottky region in the bulk.

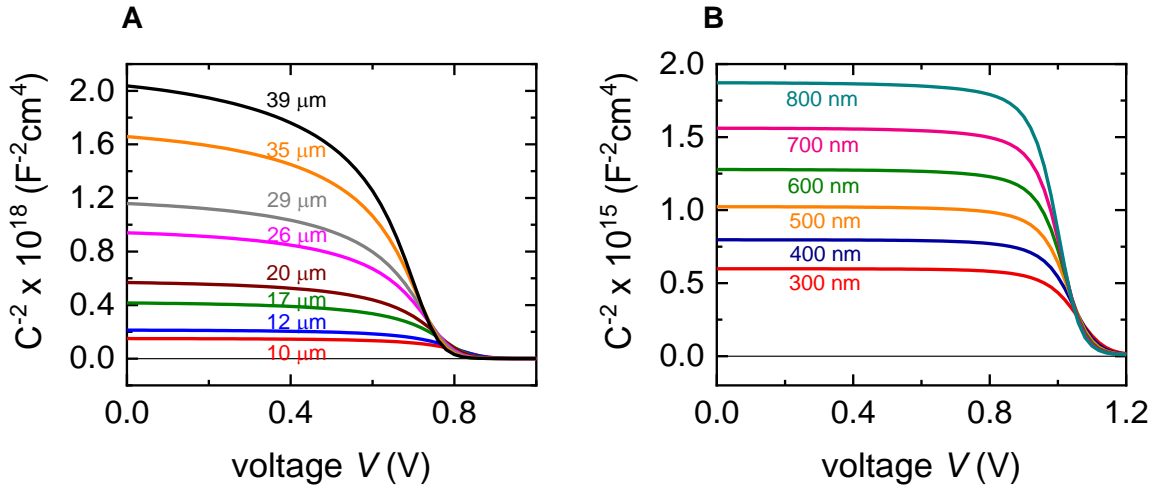


Fig. S3. Mott-Schottky plots of bulk and thin film trap-free, dopant-free perovskite solar cells. Simulated Mott-Schottky plots at 10^3 Hz of a p-i-n type perovskite solar cell with (A) varying thicknesses of the bulk perovskite layer and (B) thin film perovskite layer. These plots correspond to the capacitance-voltage simulations of Fig. 1A, B in the main text respectively.

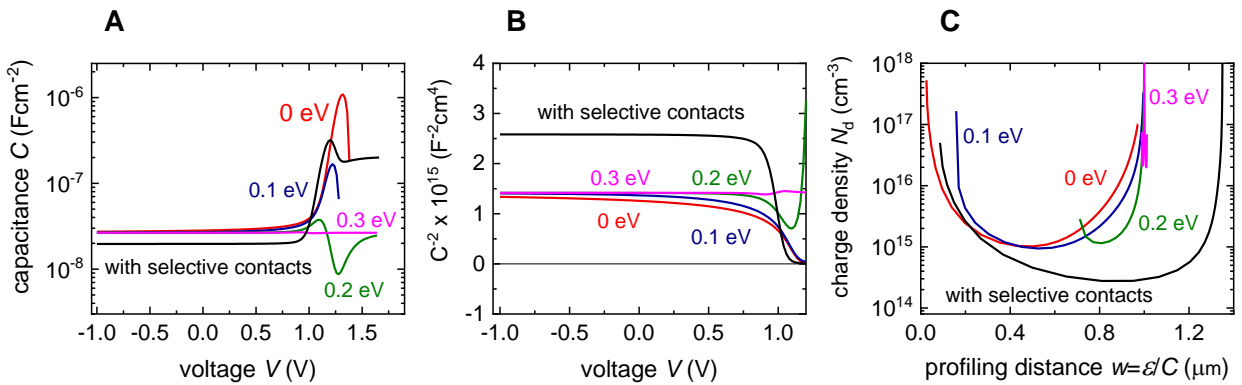


Fig. S4. Effect of selective contacts on doping profile. Simulated (A) capacitance-voltage plots (B) corresponding Mott-Schottky plots and (C) doping density profiles of a p-i-n type PTAA (10 nm)/ perovskite (1 μ m)/ PCBM (25 nm) solar cell with and without electron and hole selective contact layers (PCBM and PTAA respectively). For the case without selective contact layers, the injection barrier for electrons and holes at cathode and anode respectively are set equal and varied as shown. Smaller injection barriers show a larger contribution of the chemical capacitance due to injection of carriers at large forward bias. For large injection barriers beyond ~ 200 meV, the chemical capacitance is not seen and the response is solely from the constant geometric capacitance measured at reverse bias. This is reflected in the

doping density profiles in **C** where the apparent profiling distance is almost a constant value for the 0.3 eV barrier case but gradually scans a bigger range of apparent profiling distances for smaller barriers. Note also that the capacitance with selective contact layers is different in magnitude to that without selective contact layers, which affects the apparent profiling distance.

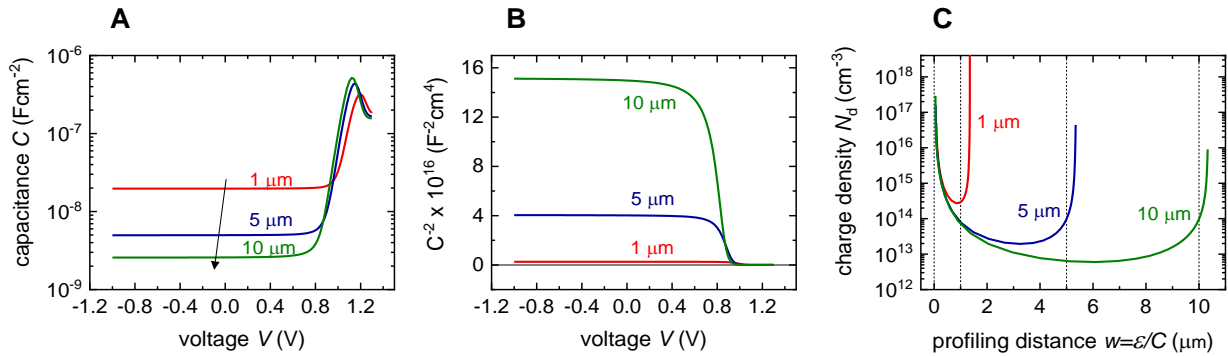


Fig. S5. Effect of geometric capacitance on doping profiles of thin film and bulk single crystal perovskite solar cells. Simulated (A) capacitance-voltage plots (B) corresponding Mott-Schottky plots and (C) doping profiles of a p-i-n type PTAA (10 nm)/ perovskite/ PCBM (25 nm) solar cell for different thicknesses of the intrinsic perovskite layer. The dashed lines in C indicate the apparent profiling distances corresponding to the thickness of each perovskite layer considered. The low bias saturation capacitance is affected by the geometric capacitance of the selective contact layers for thin films as seen in A, which leads to an overestimation of the apparent profiling distance as seen in C.

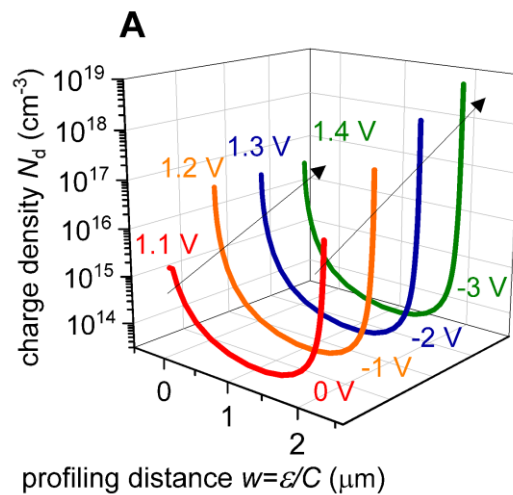


Fig. S6. Sensitivity of apparent interfacial charge densities to applied voltage in doping profiles. Evolution of apparent interfacial charge densities (sharp upward peaks) for a p-i-n type PTAA (10 nm)/perovskite (2 μm) /PCBM (25 nm) solar cell due to maximum forward and reverse bias voltage.

A1. Analytical expression for doping profile at forward bias

We consider a general capacitance of the form(15)

$$C = C_g + C_0 \exp\left(\frac{qV}{mk_B T}\right). \quad (\text{S1})$$

where $C_g = \epsilon_r \epsilon_0 / d$ is the geometric capacitance of the layer of thickness d and C_0 and m are the pre-factor and slope respectively for the diffusion capacitance that is considered proportional to the current-voltage (injection) characteristics of the diode. If the formalism developed for reverse bias capacitance is applied to this capacitance, the apparent doping density profile is given by

$$N_d = \frac{-2}{q \epsilon_r \epsilon_0} \left[\frac{dC^{-2}}{dV} \right]^{-1}, \quad (\text{S2})$$

which can be represented in terms of the slope of the capacitance versus voltage and profiling position $w = \epsilon_r \epsilon_0 / C$ as

$$N_d = \frac{\epsilon_r \epsilon_0 C}{q w^2} \left[\frac{dC}{dV} \right]^{-1}. \quad (\text{S3})$$

For large forward bias, we have

$$C \cong C_0 \exp\left(\frac{qV}{mk_B T}\right), \quad (\text{S4})$$

$$\frac{dC}{dV} = \frac{qC}{mk_B T}. \quad (\text{S5})$$

Substituting equations S4 and S5 in equation S3, we get

$$N_d(w) = \frac{mk_B T \epsilon_r \epsilon_0}{q^2 w^2}. \quad (\text{S6})$$

Equation S6 shows that $N_d \propto w^{-2}$ at large forward bias, which explains the rise in interfacial charge densities for the lowest profiling distances (i.e. close to the interface). This forms the left side of the ‘U’-shaped doping profile. The flat region in the profile can be described by a constant value $N_{d,min}$, while the constant geometric capacitance gives an infinite rise in charge densities at reverse bias, forming the right side of the ‘U’-shaped profile. Therefore, the doping profile at forward bias is given by

$$N_d(w) = N_{d,min} + \frac{mk_B T \epsilon_r \epsilon_0}{q^2 w^2}. \quad (\text{S7})$$

A2. Derivation of minimum charge density for resolution

We again consider a general capacitance

$$C = C_g + C_0 \exp\left(\frac{qV}{mk_B T}\right), \quad (\text{S8})$$

The doping density profile is given by

$$N_d = \frac{-2}{q \epsilon_r \epsilon_0} \left[\frac{dC^{-2}}{dV} \right]^{-1}. \quad (\text{S9})$$

The profiling position is given by

$$w = \frac{\epsilon_r \epsilon_0}{C}, \quad (\text{S10})$$

and at deep reverse bias, we obtain the thickness of the layer as

$$d = \frac{\epsilon_r \epsilon_0}{C_g}. \quad (\text{S11})$$

Substituting equations S8 and S11 in S9, we get

$$N_d = \frac{mk_B T \epsilon_r \epsilon_0 C^3}{q^2 d^2 C_g^2 C_0 \exp(qV/mk_B T)}. \quad (\text{S12})$$

To obtain the minimum value of the doping density, we need to solve

$$\frac{dN_d}{dw} = \frac{dN_d}{dV} \frac{dV}{dw} = 0 . \quad (\text{S13})$$

Differentiating equation S10 and S12 with respect to voltage, we obtain

$$\frac{dV}{dw} = \frac{-C^2}{\varepsilon_r \varepsilon_0 (dC/dV)} , \quad (\text{S14})$$

$$\frac{dN_d}{dV} = \frac{mk_B T \varepsilon_r \varepsilon_0}{q^2 d^2 C_g^2 C_0} \left[\frac{3C^2 (dC/dV) \exp(qV/mk_B T) - (qC^3/mk_B T) \exp(qV/mk_B T)}{\exp(2qV/mk_B T)} \right] . \quad (\text{S15})$$

Solving equation S13 using equations S8, S14 and S15, we obtain

$$C_{\min} = 3C_0 \exp(qV_{\min}/mk_B T) , \quad (\text{S16})$$

which is the minimum value of the capacitance at a corresponding voltage V_{\min} . Substituting equation S16 in equation S8, we obtain

$$C_g = 2C_0 \exp(qV_{\min}/mk_B T) . \quad (\text{S17})$$

Substituting equations S16 and S17 in equation S12 at the voltage V_{\min} , we obtain the minimum doping density as

$$N_{d,\min} = \frac{27mk_B T \varepsilon_r \varepsilon_0}{4q^2 d^2} . \quad (\text{S18})$$

References

1. J. A. Chaney, P. E. Pehrsson, Work Function Changes and Surface Chemistry of Oxygen, Hydrogen, and Carbon on Indium Tin Oxide. *Appl. Surf. Sci.* **180**, 214-226 (2001).
2. Z. Ni *et al.*, Resolving Spatial and Energetic Distributions of Trap States in Metal Halide Perovskite Solar Cells. *Science* **367**, 1352-1358 (2020).
3. S. Sami, P. A. Haase, R. Alessandri, R. Broer, R. W. Havenith, Can the Dielectric Constant of Fullerene Derivatives Be Enhanced by Side-Chain Manipulation? A Predictive First-Principles Computational Study. *J. Phys. Chem. A* **122**, 3919-3926 (2018).
4. M. Sendner *et al.*, Optical Phonons in Methylammonium Lead Halide Perovskites and Implications for Charge Transport. *Mater. Horiz.* **3**, 613-620 (2016).
5. Z. Liu *et al.*, Open-Circuit Voltages Exceeding 1.26 V in Planar Methylammonium Lead Iodide Perovskite Solar Cells. *ACS Energy Lett.* **4**, 110-117 (2018).
6. J. H. Noh, S. H. Im, J. H. Heo, T. N. Mandal, S. I. Seok, Chemical Management for Colorful, Efficient, and Stable Inorganic–Organic Hybrid Nanostructured Solar Cells. *Nano Lett.* **13**, 1764-1769 (2013).
7. J. Maibach, E. Mankel, T. Mayer, W. Jaegermann, The Band Energy Diagram of PCBM–DH6T Bulk Heterojunction Solar Cells: Synchrotron-Induced Photoelectron Spectroscopy on Solution Processed DH6T: PCBM Blends and in Situ Prepared PCBM/DH6T Interfaces. *J. Mater. Chem. C* **1**, 7635-7642 (2013).
8. A. Magomedov *et al.*, Self-Assembled Hole Transporting Monolayer for Highly Efficient Perovskite Solar Cells. *Adv. Energy Mater.* **8**, 1801892 (2018).
9. S. Cook, R. Katoh, A. Furube, Ultrafast Studies of Charge Generation in PCBM: P3HT Blend Films following Excitation of the Fullerene PCBM. *J. Phys. Chem. C* **113**, 2547-

2552 (2009).

10. Y. Kim *et al.*, Composition and Annealing Effects in Polythiophene/Fullerene Solar Cells. *J. Mater. Sci.* **40**, 1371-1376 (2005).
11. F. Staub *et al.*, Beyond Bulk Lifetimes: Insights into Lead Halide Perovskite Films from Time-Resolved Photoluminescence. *Phys. Rev. Appl.* **6**, 044017 (2016).
12. L. M. Herz, Charge-Carrier Mobilities in Metal Halide Perovskites: Fundamental Mechanisms and Limits. *ACS Energy Lett.* **2**, 1539-1548 (2017).
13. E. Von Hauff, V. Dyakonov, J. Parisi, Study of Field Effect Mobility in PCBM Films and P3HT: PCBM Blends. *Sol. Energy Mater. Sol. Cells* **87**, 149-156 (2005).
14. S. Barard *et al.*, Separate Charge Transport Pathways Determined by the Time of Flight Method in Bimodal Polytriarylamine. *J. Appl. Phys.* **105**, 013701 (2009).
15. S. M. Sze, K. K. Ng, *Physics of Semiconductor Devices* (John Wiley & sons, 2006), pp.100-102.